ISBN: 978-1-925627-03-9

Air Entrainment Rate in Vertical Planar Plunging Jets

Rui Shi[1], Hang Wang[2], Hubert Chanson[3]

[1]Research student, The University of Queensland, Brisbane QLD, Australia

[2]Research Fellow, The University of Queensland, Brisbane QLD, Australia
E-mail: hang.wang@uqconnect.edu.au

[3]Professor, The University of Queensland, Brisbane QLD, Australia

Abstract

This paper presents an experimental study of air entrainment in vertical plunging jets. The inflow was a quasi-two-dimensional supported planar water jet, discharging from a rectangular nozzle into a large-size receiving pool at rest. With impact velocities between 2.5 m/s and 6.0 m/s, substantial air bubble entrainment was observed at the impingement point, while pre-entrainment in the falling jet free-surface was associated with large jet disturbance. The void fraction and interfacial velocity distributions were measured using dual-tip phase-detection probes. The results enabled accurate calculation of air entrainment rate, a parameter relevant to many water engineering applications. The results are compared with previous investigations, highlighting the significance of the impact velocity on the air entrainment capacity in a plunging jet flow.

1. INTRODUCTION

When a high-speed water jet plunges into a receiving pool, air entrainment may take place at the jet-pool intersection when the jet impact velocity exceeds a critical value of onsite velocity (Bin 1993, Ervine 1998). In nature, the air entrainment phenomenon at plunging jets may influence the ecosystem by increasing the oxygen level in water body. Artificial plunging jet flows are also widely utilised in various engineering applications (McKeogh & Ervine 1981). For example, in fish farming and wastewater treatment industries, plunging jets are deployed as an efficient device to enhance air-water mixing. In many occasions, entrainment of air needs to be carefully controlled or minimised, like in chemical reactors, carbonated beverage industry and nuclear reactor containment cooling systems. For all these applications, the air entrainment rate is a key design and operation parameter, which is determined by the void fraction and velocity distributions in the air-water flow. The air-water flow properties in the near-flow field of a plunging jet vary for different flow conditions including the jet impact velocity, jet length and jet disturbance (Kiger & Duncan 2012). For a relatively high impact velocity, turbulent flow structures develop at various length and time scales and interact intensively with the entrained air bubbles, limiting the flow measurement techniques applicable in the subsurface two-phase flow region. An effective instrument is the intrusive phase-detection probe broadly used in air-water open channel flows (Chanson 2002). It has been used successfully in plunging jet investigations by Cummings & Chanson (1997a), Brattberg & Chanson (1998), Bertola et al. (2017). Numerical study of air entrainment in plunging jets was restricted either at low Reynolds numbers or at scales greater than the majority bubble sizes (Brouilliot & Lubin 2013). Simultaneous simulation of bubble deformation and turbulence field is still of great challenge, and benchmark physical data are urgently needed for numerical model verification.

The paper presents a new experimental study of two-dimensional vertical plunging jets, with a focus on quantification of air entrainment rate for different impact velocities. Air flux was calculated based upon detailed void fraction and bubble velocity data measured on the jet centreline. Comparison was made between present and previous data sets, and a discussion is developed on analytical prediction of air entrainment rate based upon experimental calibration.

2. EXPERIMENTAL SETUP

2.1. Experimental Facility

The investigated jet flow was a vertical quasi-two-dimensional water jet, issued from a rectangular nozzle into a large receiving tank. The jet nozzle was 0.269 m wide, with a fixed opening d_o = 0.012 m. A PVC sheet extended from the nozzle edge to support the planar jet with an angle of 88.5° with the horizontal (Fig. 1a). The jet support was 0.35 m long and equipped with a side window to facilitate flow visualisation. Herein we use coordinate *x* to denote the longitudinal distance from the nozzle edge and *y* for the distance normal to the jet support. For all investigated jet conditions, the length of falling jet was set at x_1 = 0.1 m. That is, the impingement point was 0.1 m below the nozzle, and the jet support ended at further 0.25 m beneath the impingement point (Fig. 1a). The receiving tank was 1.5 m deep, 2.5 m long, and 1 m wide, ensuring that the two-phase plunging jet flow was not affected by the pool boundaries. The water level in the tank was controlled with a sharp-crested weir at the far end. Water was supplied either from a constant head tank when the flow rate was less than 0.0137 m^3/s or from a high-head pump for larger discharges up to 0.038 m^3/s. The water was fed into the nozzle through a vertical pipeline that first divided the pipe flow into two horizontal branch pipes then mixed the horizontal flows at a T-junction upstream of the nozzle (Fig. 1b). Some mesh roller was installed in the T-junction to facilitate flow stabilisation. Air-water flow measurements close to the jet nozzle indicated no aeration taking place in the pipeline prior to nozzle discharge. The flow rate was measured using an orifice meter or Venturi meter, calibrated with a volume per time technique. The flow rate reading was checked against the calculation of mass conservation based on velocity and void fraction measurements in the jet, showing satisfactory accuracy.

The translation of flow-measuring probes in the longitudinal and normal directions relative to the jet was controlled with two fine-adjustment travelling mechanisms. The probe position was read from two linear position sensors that provided accuracy within 0.05 mm.

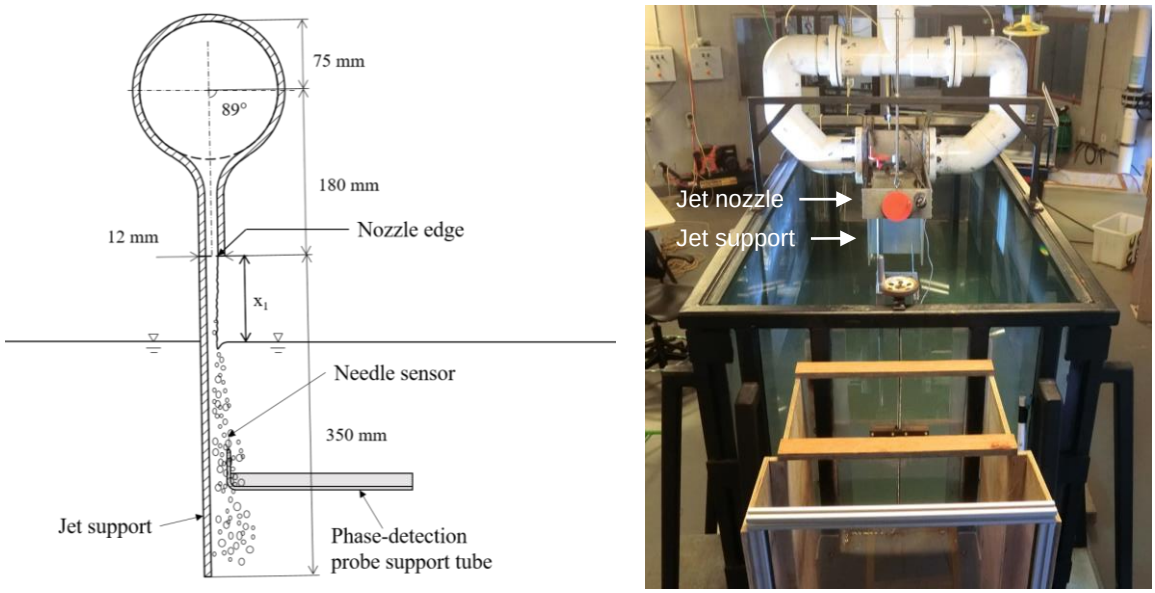

Figure 1 – Experimental setup: (a, left) Sideview sketch of jet nozzle, jet support and position of phase-detection probe; (b, right) Front-view photograph of supply pipeline and receiving tank.

2.2. Measurement of Air Flux

A series of dual-tip phase-detection probes were used for air-water flow measurements. The probes were manufactured and validated at The University of Queensland. Each dual-tip probe was equipped with two needle sensors with different lengths. The two sensors were mounted parallel to each other and against the main flow direction. The leading sensor tip was Δx (m) ahead the trailing sensor tip in the longitudinal direction. While in air-water flow, the sensors detected air-water interfaces based on the instantaneous change in electric conductivity of the ambient fluid covering the sensor tip, and the recorded voltage signal was proportional to the instantaneous void fraction. Both sensors were stimulated simultaneously at 20 kHz for 90 s. The time-averaged void fraction *C* was derived from

binarised probe signal for the sampling duration. The signal binarisation was carried out using a 50% threshold between the maximum air and water sample probabilities. Given a large enough number of air-water interfaces detected by both leading and trailing sensors, a correlation analysis between the raw (un-binarised) signals of the two sensors provided the average time lag of a flow structure travelling between the sensor tips. The time-averaged velocity V was calculated as

$$V = \frac{\Delta x}{T} \quad (1)$$

where T is the time lag of the maximum cross-correlation coefficient. The velocity V given by equation (1) is the longitudinal component of the air-water interfacial velocity, which equals to the longitudinal flow velocity in high-speed flows. The air flux q_{air} was calculated as

$$q_{air} = \int_0^Y CV dy \quad (2)$$

at different cross-sections on the jet centreline, where y is the normal coordinate with y = 0 at the jet support. The upper limit of integration Y equals Y_{90} in the free-falling jet and $+\infty$ in the plunging pool, where Y_{90} is a characteristic position with the void fraction C = 90%. In the present study, measurements of void fraction and interfacial velocity were repeated with six phase-detection probes with different Δx = 2.4 mm, 4.9 mm, 7.1 mm, 9.9 mm, 16.0 mm and 25.0 mm, and ensemble-averaged results were presented to minimise any impact of measurement errors.

2.3. Experimental Flow Conditions

In the present experimental facility, the critical velocity V_e of bubble entrainment onset was observed to be between 1.5 m/s and 1.6 m/s for the fixed jet length x_1 = 0.1 m. Three jet impact velocities were investigated: V_1 = 2.5 m/s, 4.0 m/s and 6.0 m/s, the corresponding nozzle velocities being V_o = 2.07 m/s, 3.75 m/s and 5.83 m/s, respectively. Table 1 summarises the experimental flow conditions, where d_1 is the jet thickness at impingement given by the continuity and Bernoulli principles.

Table 1 – Experimental flow conditions

Q (m^3/s)	d_o (m)	V_o (m/s)	x_1 (m)	V_1 (m/s)	d_1 (m)	Fr (-)	Re (-)	We (-)
0.0067	0.012	2.07	0.1	2.5	0.0099	3.2	24,750	860
0.0121	0.012	3.75	0.1	4.0	0.0113	7.5	45,200	2,510
0.0188	0.012	5.83	0.1	6.0	0.0117	13.3	70,200	5,850

Notes: Q: water discharge; d_o: nozzle opening; V_o: nozzle velocity; x_1: jet length; V_1: jet impact velocity; d_1: jet thickness at impingement; Fr: Froude number $Fr = (V_1\text{-}V_e)/(gd_1)^{0.5}$; Re: Reynolds number $Re = \rho V_1 d_1/\mu$; We: Weber number $We = \rho V_1^2 d_1/\sigma$

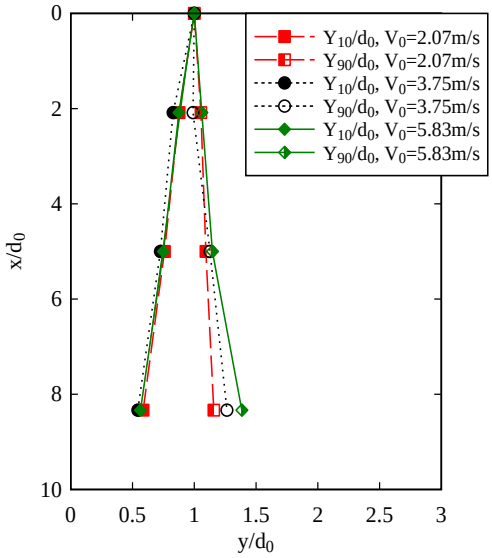

Figure 2 – Longitudinal broadening of air-water mixing layer at falling jet free-surface.

All free-falling jets were partially-developed at impingement with a thin boundary layer next to the jet support. The jet surface was visually rough. Free-surface air entrainment took place immediately downstream of the jet nozzle, and the air-water mixing layer broadened rapidly along the jet because of the development of jet surface disturbance. Figure 2 shows the longitudinal broadening of the air-water mixing layer between characteristic positions Y_{10} and Y_{90} where the local void fraction equals 10% and 90% respectively. The jet surface disturbance was likely associated with the presence of instationary three-dimensional flow structures in the jet. Free-surface measurements showed slightly larger jet thickness on the centreline than close to the lateral sidewalls of jet support, and this non-uniformity in spanwise jet thickness distribution developed with increasing distance from the jet nozzle. Large free-surface fluctuations were observed together with the surface air-water exchange. The free-falling jets were pre-aerated prior to the impingement point, and the contribution of pre-entrainment to the total air entrainment of plunging jet must be considered.

3. RESULTS

3.1. Void Fraction

A turbulent impinging flow entrains air at impingement primarily with the generation and detachment of air cavities at the free-surface discontinuity (Cummings & Chanson 1997b). The elongated air cavities formed enclosed air packets that were advected downstream and quickly broken up into smaller bubbles by turbulent shear. The transport of air bubbles in the turbulent shear flow region underneath the impingement point was an advective diffusion process. This may be seen from the streamwise evolution of void fraction distributions, as presented in Figure 3. Figure 3 shows the time-averaged void fraction which is the ensemble-averaged value of the data. For each jet impact velocity V_1, the data are plotted at five cross-sections between immediately below the impingement point and the end of jet support.

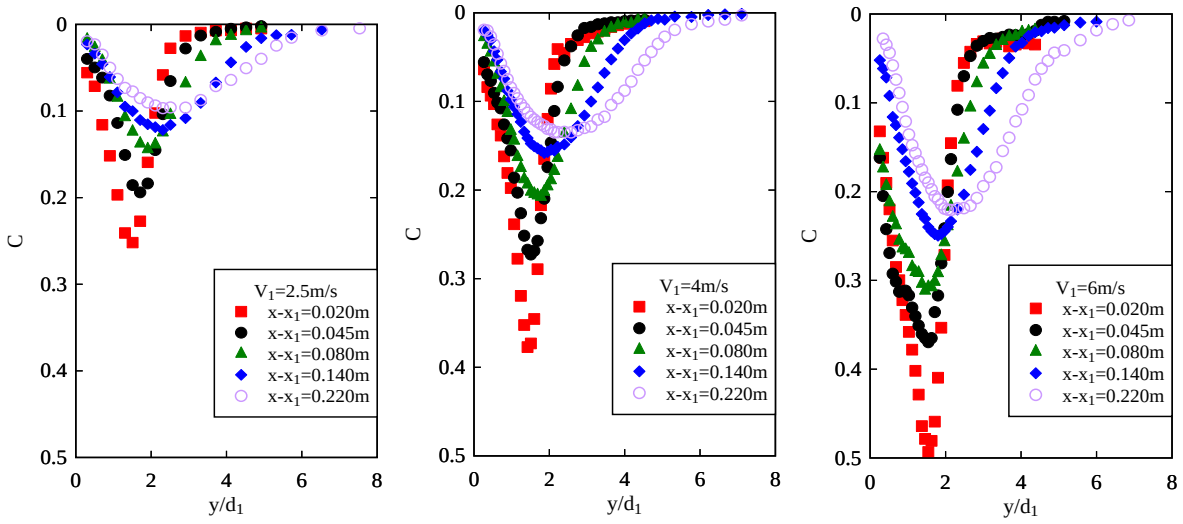

Figure 3 – Time-ensemble-averaged void fraction distributions in plunging pool: (a, left) V_1 = 2.5 m/s; (b, middle) V_1 = 4.0 m/s; (c, right) V_1 = 6.0 m/s.

A typical time-averaged void fraction profile exhibited a bell-shape or quasi-Gaussian distribution. That is, with increasing distance y from the jet support, the void fraction increased first to a maximum value C_{max} and gradually decreased to zero in the ambient un-aerated water. While the bubbles were advected in the vertical direction against buoyancy, the diffusion layer was broadened, and the void fraction profiles became flat with a decreasing maximum value. The longitudinal decay of C_{max} followed a power relationship: $C_{max} \propto (x\text{-}x_1)^{-a}$, the value of *a* typically between 0.3 and 0.6, and was a function of the jet impact velocity V_1. For a larger impact velocity, the maximum void fraction was larger at a given cross-section, and it took a longer distance to decrease to zero. With the longitudinal broadening of the bubble advection layer, the horizontal position of the maximum void fraction Y_{Cmax} shifted away from the jet support.

Further statistical analysis of individual bubble detections indicated that the advected bubbles experienced break-up, coalescence, collapse and re-grouping when interacting with the turbulent shear flow before they reached stagnation over the penetration depth, dispersed into surrounding water or rose upwards. These were reflected by the longitudinal evolutions of bubble count rate, bubble size probability spectra, and occurrence frequency and average size of bubble clusters. The results are not

shown.

3.2. Interfacial Velocity

The velocity of entrained bubbles showed a transverse distribution characteristic of a free shear layer. Figure 4 presents the ensemble-averaged experimental data corresponding to the same flow conditions as Figure 3. The maximum velocity V_{max} was seen close to the jet support, and the velocity decreased monotonically with increasing normal distance from the support plane at a given cross-section. Negative velocity ($V_{recirc} < 0$) was detected on the still-water side of the shear layer, linked to the upward recirculating bubbly motion. The recirculation velocity V_{recirc} appeared to be constant at different vertical positions. In the transition region between positive and negative flows, the largest velocity gradient was observed at the location $y_{0.5}$, where $V(y_{0.5}) = (V_{max}-V_{recirc})/2$. This position was further away from the jet support compared to the position of maximum void fraction, i.e. $Y_{Cmax} < y_{0.5}$. With dual-tip phase detection probes, data scatter was often observed in this transition region because of the limitation of cross-correlation analysis when the instantaneous velocity fluctuated between positive and negative values. Interestingly, little impact of the sensor-tip separation distance Δx (herein 2.4 mm < Δx < 25.0 mm) was seen in terms of the velocity measurement results.

All plunging jet flows experienced some longitudinal deceleration. For the three impact velocities V_1 = 2.5 m/s, 4 m/s and 6 m/s in Figure 4, the ratio of maximum velocity to impact velocity V_{max}/V_1 dropped from unity down to 0.57, 0.70 and 0.82 respectively, at the longitudinal position x-x_1 = 0.22 m.

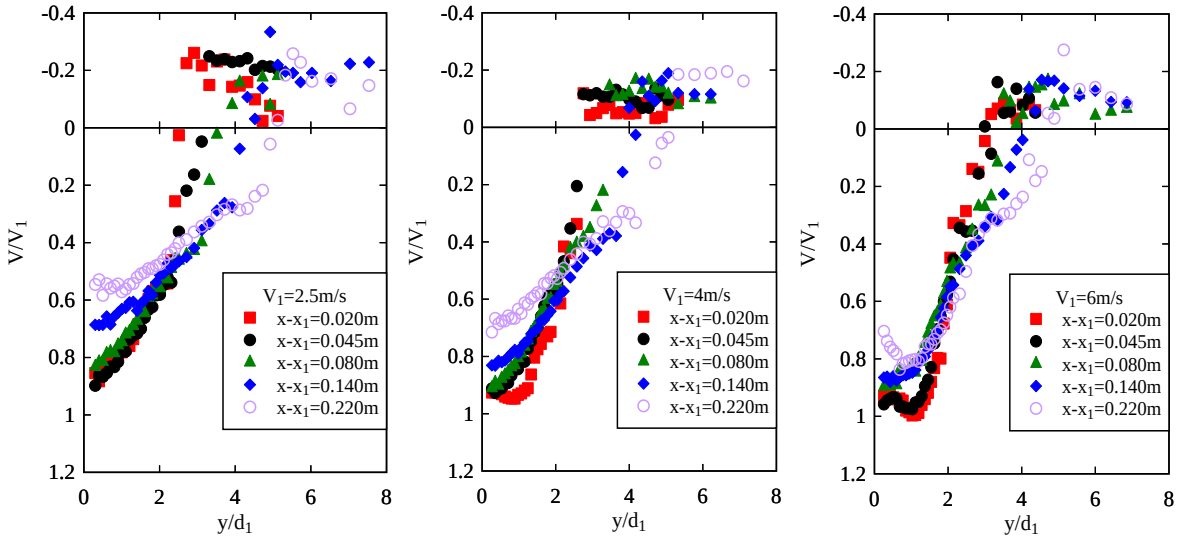

Figure 4 – Time-ensemble-averaged longitudinal interfacial velocity distributions in plunging pool: (a, left) V_1 = 2.5 m/s; (b, middle) V_1 = 4.0 m/s; (c, right) V_1 = 6.0 m/s.

3.3. Air Entrainment Rate

The air flux was calculated using equation (2) for each phase-detection probe data set, and the results were ensemble-averaged (Fig. 5). Figure 5a shows the dimensionless air flux q_{air}/q_w at various longitudinal locations. The pre-entrainment rate in the jet is shown for completeness, i.e. x-x_1 < 0.

First the results showed substantial pre-entrainment in the jet (x-x_1 < 0). Since the pre-entrained air flux was integrated from y = 0 to $y = Y_{90}$, a large jet surface roughness led to a thick air-water mixing layer for 0 < y < Y_{90} (Fig. 2), contributing to a high air flux next to the jet free-surface. Physically, it is believed that the pre-entrained air flux associated with jet surface fluctuations was not advected into deep water. Instead, it only affected the total air entrainment rate within a very-short distance below the impingement point, e.g. 0 < (x-x_1)/d_1 < 5 to 10 for V_1 = 2.5 to 6 m/s (Fig. 5a). Within this distance, the air-water flow was detrained rapidly. This was not observed in previous studies where the contribution of jet pre-entrainment was much less significant (e.g. Brattberg & Chanson 1998). Further downstream, the majority of air bubbles were advected by large turbulent vortical structures, and the air flux corresponded largely to the singular air entrapment at the impingement point. Such air flux maintained a constant level for 5 to 10 < (x-x_1)/d_1 < 22, suggesting little detrainment of the bubbly flow over this distance. This was consistent with the finding of Brattberg & Chanson (1998) for 0 < (x-x_1)/d_1 < 17. Figure 5a further shows

an increasing air entrainment capacity for an increasing impact velocity V_1, for a given jet length.

Figure 5b compares the present air entrainment rate data at a given location $(x\text{-}x_1)/d_1 = 7.5$ with the data of Cummings & Chanson (1997a), Brattberg & Chanson (1998) and Bertola et al. (2017), as a function of the Froude number defined as $Fr_1 = (V_1\text{-}V_e)/(gd_1)^{0.5}$. The results showed comparable quantitative values between all data sets, with an increasing air entrainment rate with increasing Froude number. The air entrainment rate at the smallest tested impact velocity V_1 = 2.5 m/s was however larger compared to the increasing trend for V_1 < 4 m/s, as observed to be different from the increasing trend for V_1 > 4 m/s by several studies (Van De Sande & Smith 1973, Sene 1988, Brattberg & Chanson 1998). It is conceivable that the jet pre-aeration might have played an important role in the present experiments.

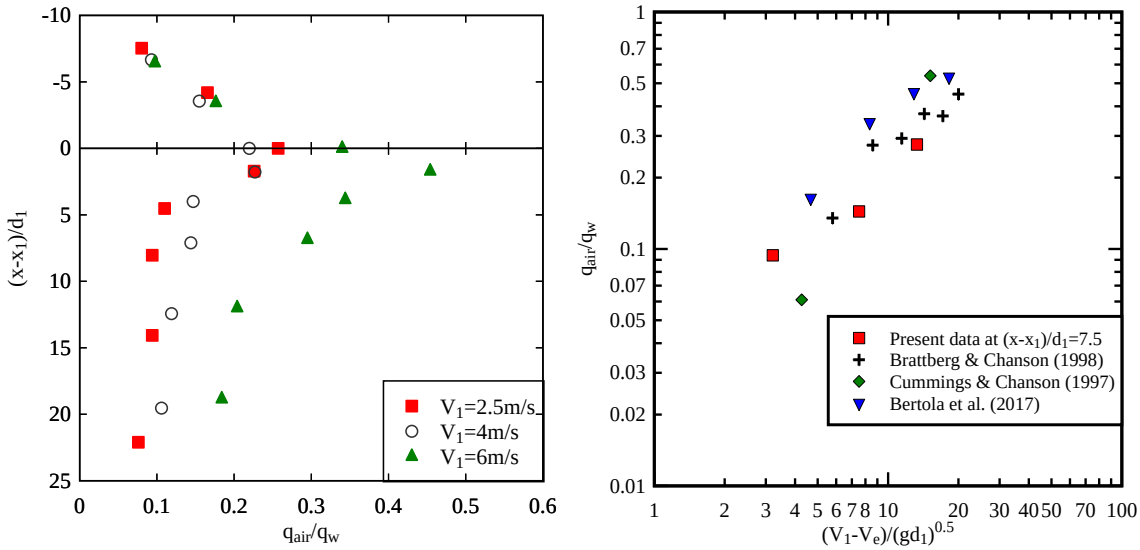

Figure 5 – Ensemble-averaged air entrainment rate: (a, left) Longitudinal variation in free-falling jet and plunging pool for different impact velocities; (b, right) Effects of dimensionless impact velocity, with comparison to data of Brattberg & Chanson (1998), Cummings & Chanson (1997a) and Bertola et al. (2017).

3.4. Discussion: Analytical Model of Air Entrainment Rate

Considering a simplified two-dimensional vertical plunging jet, the impingement point acts as a point source of entrained air bubbles, and the bubbles were advected vertically downstream while being diffused in normal directions. The local void fraction distribution at a given longitudinal position $(x\text{-}x_1)/d_1$ in the plunging pool can be modelled by solving the advective diffusion equation for air bubbles:

$$\frac{V_1}{D_t}\frac{\partial C}{\partial x} = \frac{\partial^2 C}{\partial y^2} \tag{3}$$

where D_t is a bubble diffusivity assumed independent of the horizontal position y (Chanson 1997). The analytical solution of equation (3) may be applied to a supported plunging jet using the method of image, yielding:

$$C = \frac{q_{air}}{q_w}\frac{\frac{Y_{C_{max}}}{d_1}}{\sqrt{4\pi D^{\#}\frac{x-x_1}{d_1}}}\left(\exp\left(-\frac{1}{4D^{\#}}\frac{\left(\frac{y-Y_{C_{max}}}{d_1}\right)^2}{\frac{x-x_1}{d_1}}\right)+\exp\left(-\frac{1}{4D^{\#}}\frac{\left(\frac{y+Y_{C_{max}}}{d_1}\right)^2}{\frac{x-x_1}{d_1}}\right)\right) \tag{4}$$

with $D^{\#}$ the dimensionless diffusivity: $D^{\#} = D_t/(V_1 d_1)$ (Cummings & Chanson 1997b). Practically, for given jet flow conditions, the experimental data provide the local maximum void fraction C_{max} and its position Y_{Cmax}. The diffusivity coefficient derives from the best fit of equation (4) to the physical data at a position $(x\text{-}x_1)/d_1$. In turn, the following relationship between the maximum void fraction and air entrainment flux holds:

$$\frac{q_{air}}{q_w} = C_{max} \sqrt{4\pi D^{\#} \frac{x - x_1}{d_1}} \Big/ \frac{Y_{C_{max}}}{d_1} \quad (5)$$

In equation (5), C_{max}, Y_{Cmax}/d_1 and $D^{\#}$ are all functions of the longitudinal position $(x\text{-}x_1)/d_1$, and C_{max} and $D^{\#}$ further vary for different jet impact velocities. Figure 6 compares the air entrainment rate calculated by equation (5) with the experimental data shown in Figure 5. The prediction of void fraction distribution (eq. (5)) was consistently larger than the integration of void fraction and velocity (eq. (2)). The best agreement was achieved at the position immediately below the plunge point. The reason for the discrepancy between the two approaches was not obvious. A possible explanation could be that equation (4) was derived based on the assumption of a uniform velocity distribution, whereas the actual velocity field in equation (2) was characterised by a marked velocity gradient in the shear layer.

An improved accuracy of air entrainment rate prediction may be achieved by considering both the analytical expressions of void fraction and velocity. Experimental results showed that the velocity distribution followed a modified solution of the equation of motion in a free shear layer:

$$\frac{V - V_{recirc}}{V_{max} - V_{recirc}} = \frac{1}{2}\left(1 - \text{erf}\left(K \frac{y - y_{0.5}}{x - x_1}\right)\right) \quad (6)$$

where K is a coefficient deriving from the assumption of a constant eddy viscosity across the shear layer. In equation (6), the dimensionless maximum velocity V_{max}/V_1 decreases longitudinally, the rate of decrease being affected by the impact velocity, while the dimensionless position $y_{0.5}/d_1$ and coefficient K follows linear increasing trends with increasing distance $(x\text{-}x_1)/d_1$, independent of the impact velocity. A combination of equations (4) to (6) provides an analytical expression of air entrainment flux in plunging jet as a function of the streamwise position. In such a model, a series of characteristic parameters need to be calibrated using experimental data, including C_{max}, Y_{Cmax}/d_1, $D^{\#}$, V_{max}/V_1, $y_{0.5}/d_1$ and K, among which C_{max}, $D^{\#}$ and V_{max}/V_1 are further functions of jet conditions like impact velocity V_1.

A similar approach was proposed by Wang & Chanson (2017) for horizontal hydraulic jumps, where the void fraction distribution followed the singular entrainment solution of equation (3) in the shear flow region and interfacial entrainment solution in the upper free-surface region, with the velocity distribution modelled by wall jet equation. A key finding of their work was that the characteristic parameters used to determine the void fraction and velocity profiles exhibited self-similar distributions within the length of jump roller which was a function of the Froude number. As a result, the spatial distributions of void fraction and velocity could be determined by the Froude number of the flow based on a series of empirical relationships deriving from experiments. Therefore, the air entrainment rate was predictable. Although some common features of air entrainment are shared between hydraulic jump and plunging jet, such self-similarities were not found in plunging jets, preventing further validation of a general analytical model for air entrainment rate in plunging jets.

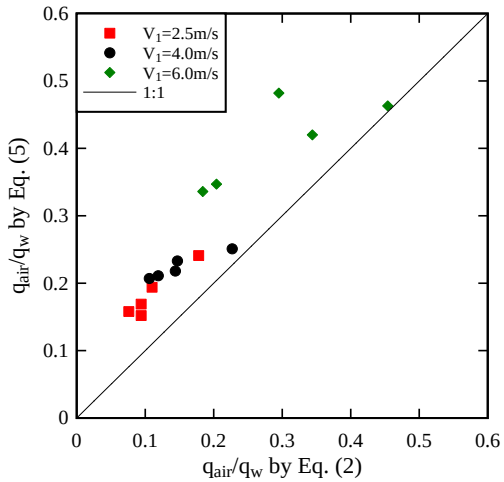

Figure 6 – Comparison between air entrainment rates calculated using equations (2) and (5).

4. CONCLUSION

New experiments of air-water flow measurements in vertical planar plunging water jets were conducted. Void fraction and longitudinal interfacial velocity were measured, and air entrainment rate was calculated on the jet centreline. Six different phase-detection probes were used, and the ensemble-averaged results were presented. While the overall void fraction and velocity measurement results were consistent between different probes, the ensemble-averaging reduced the velocity data scatter in the transition region between downward and upward bubbly flows, providing a more accurate air flux quantification.

The present plunging jet setup was characterised by relatively large jet disturbance and pre-entrainment at the jet free-surface. The longitudinal evolution of void fraction and velocity distributions in the plunging pool characterised the streamwise broadening of bubble diffusion layer and turbulent shear layer, which did not coincide with each other. A larger jet impact velocity resulted in higher void fraction at a given depth and a slower deceleration of the flow, thus a higher air entrainment rate. The air entrainment rate decreased within a short distance below the impingement point where the effects of jet pre-entrainment were significant, while it maintained a constant level at further downstream corresponding to the advection of bubbles entrained at the plunge point and carried by large turbulent structures. The effects of Froude number on air entrainment rate compared well with previous studies for impact velocities greater than 4 m/s. For $V_1 < 4$ m/s, the air entrainment rate was higher, likely because of the impact of high pre-entrainment rate in the jet.

5. ACKNOWLEDGMENTS

The authors thank Dr Gangfu Zhang (The University of Queensland) for allowing access to his data processing tools. The technical support of Jason Van Der Gevel and Matthew Stewart (The University of Queensland) is acknowledged. The research is supported financially by the Australian Research Council (ARC DP120100481) and the University of Queensland.

6. REFERENCES

Bertola, N.J., Wang, H. and Chanson, H. (2017), *Air Bubble Entrainment at Vertical Plunging Jets: a Large-Scale Experimental Study*, Hydraulic Model Report No. CH104/17, School of Civil Engineering, The University of Queensland, Brisbane, Australia, 256 pages.

Bin, A. (1993), *Gas Entrainment by Plunging Liquid Jets*, Chem. Eng. Sci., 48(21), 3585-3630.

Brattberg, T. and Chanson, H. (1998), *Air Entrapment and Air Bubble Dispersion at Two-Dimensional Plunging Water Jets*, Chem. Eng. Sci., 53(24), 4113-4127.

Brouilliot, D. and Lubin, P. (2013), *Numerical Simulations of Air Entrainment in a Plunging Jet of Liquid*, Journal of Fluids and Structures, 43, 428-440.

Chanson, H. (1997), *Air Bubble Entrainment in Free-Surface Turbulent Shear Flows,* Academic Press, London, UK, 401 pages.

Chanson, H. (2002), *Air-Water Flow Measurements with Intrusive Phase-Detection Probes. Can We Improve their Interpretation?* Journal of Hydraulic Engineering, 128(3), 252-255.

Cummings, P.D. and Chanson, H. (1997a), *Air Entrainment in the Developing Flow Region of Plunging Jets – Part 2: Experimental,* J. Fluids Eng., 119(3), 603-608 (DOI: 10.1115/1.2819287).

Cummings, P.D. and Chanson, H. (1997b), *Air Entrainment in the Developing Flow Region of Plunging Jets. Part 1: Theoretical Development*, J. Fluids Eng., 119(3), 597-602 (DOI: 10.1115/1.2819286).

Ervine, D.A. (1998), *Air Entrainment in Hydraulic Structures: a Review*, Proceedings of Institution of Civil Engineers, Water, Maritime & Energy, UK, 130(Sept.), 142-153.

McKeogh, E.J. and Ervine, D.A. (1981), *Air Entrainment Rate and Diffusion Pattern of Plunging Liquid Jets*. Chem. Eng. Sci., 36, 1161-1172.

Kiger, K. and Duncan, J. (2012), *Air-Entrainment Mechanisms in Plunging Jets and Breaking Waves*, Annu. Rev. Fluid Mech., 44, 563-596.

Sene, K.J. (1988), *Air Entrainment by Plunging Jets*, Chem. Eng. Sci., 43(10), 2615-2623.

Van de Sande, E. and Smith, J.M. (1973), *Surface Entrainment of Air by High Velocity Water Jets*, Chem. Eng. Sci., 28, 1161-1168.

Wang, H. and Chanson, H. (2017), *Estimate of Void Fraction and Air Entrainment Flux in Hydraulic Jump Using Froude Number,* Canadian Journal of Civil Engineering, in press (DOI: 10.1139/cjce-2016-0279).